Termination of Cryogenian ironstone deposition by deep ocean euxinia
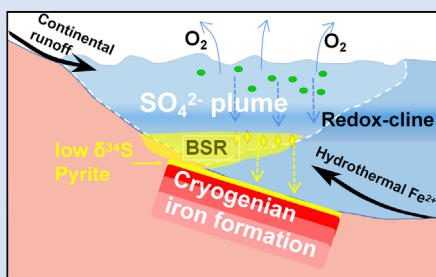
C. Wu[1], T. Yang[1], G.A. Shields[2], X. Bian[1], B. Gao[1], H. Ye[1], W. Li[1*]

OPEN ACCESS

Abstract

doi: 10.7185/geochemlet.2025

Widespread deposition of iron-rich sedimentary rocks (ironstones) occurred during the Sturtian ice age, the earlier of two Cryogenian 'Snowball Earth' glaciations. However, the reasons for the termination of Cryogenian Iron Formation (CIF) deposition remain poorly understood. Here we report a multi-isotope (Fe-C-S) study of the Xinyu CIF in South China that can directly address this question. The isotopic compositions of these multivalent elements exhibit remarkable covariance at the top of the Xinyu CIF that reflects progressive redox stratification during iron oxide deposition. Iron oxide deposition ended abruptly due to the titration of ferrous iron as pyrite following a large influx of riverine sulfate. Although termination of CIF deposition is commonly attributed to oxygenation, our data show that at least in some Cryogenian ocean basins, CIF deposition ended with the spread of euxinic rather than oxygenated waters.

Introduction

The Cryogenian Period (*ca.* 720–635 Ma) marks a turning point in the history of Earth's surficial environment, when seawater changed from a generally anoxic, ferruginous and sulfate-poor state (Canfield *et al.*, 2008; Guilbaud *et al.*, 2015) to a more oxygenated, Fe-poor and sulfate-rich state (Sahoo *et al.*, 2012; Shields *et al.*, 2019) that progressively came to dominate through the ensuing Phanerozoic Eon (Och and Shields-Zhou, 2012). Iron formations were deposited globally during the Cryogenian Period, following an interval of over 1 billion years, during which iron formations were rare (Cox *et al.*, 2013; Hoffman *et al.*, 2017), but not entirely absent (Canfield *et al.*, 2018). Iron formation deposition requires a reduced ocean to allow effective transport of iron in its soluble form, Fe^{2+}, as well as a mechanism for oxidation of the Fe^{2+} and accumulation of large masses of Fe oxides/hydroxides. Reappearance of widespread iron deposits during the Cryogenian Period has been taken, therefore, as supporting evidence for the "Snowball Earth" hypothesis, as global ice sheet cover could have led to widespread ocean anoxia (Hoffman and Schrag, 2002; Kirschvink, 1992). The appearance of Cryogenian iron formations (CIFs) provides robust evidence for the return of Fe(II)-rich, anoxic oceans, and by the same token, termination of CIF deposition was likely linked to some fundamental change in ocean chemistry.

Was disappearance of the CIFs caused by a decrease in Fe^{2+} concentration due to ocean oxygenation as seen in modern oceans? Or was it caused by the depletion of free oxygen and development of euxinic (H_2S-rich) environments as

has been proposed for the Mesoproterozoic (Canfield, 1998) and Ediacaran oceans (Li *et al.*, 2010)? The details of CIF termination bear on our understanding of the chemistry of Cryogenian oceans, and are critical for a better understanding of the biological radiations and diversification that followed. However, the termination of CIF deposition, its cause and related environmental implications, have been little discussed to date (Cox *et al.*, 2013). Iron, carbon and sulfur are major players in natural redox processes and show significant isotopic differences between their reduced and oxidised forms. In this study, we present an integrated study of C-S-Fe isotope data from a new drill core record for a large Sturtian-aged CIF from South China that was deposited in a deep marine setting. The completeness of the drill core record is unprecedented for Cryogenian iron formations and the isotopic signatures hold clues about the onset, development, and particularly, termination of CIF deposition.

Clues from a Deep Water Cryogenian Iron Formation

The CIF from Xinyu, Jiangxi Province, China presents a remarkable opportunity to study ocean chemistry during the Cryogenian glaciation (Tang *et al.*, 1987; Zhu *et al.*, 2019). The southern margin of the Yangtze Craton of South China hosts a number of stratigraphically correlative CIFs that are associated with successions assigned to the ~55 Myr, early Cryogenian 'Sturtian' ice age (Figs. 1, S-1). The Xinyu CIF, which is the largest among the South China deposits, was deposited offshore

1. State Key Laboratory for Mineral Deposits Research, School of Earth Sciences and Engineering, Nanjing University, Nanjing, Jiangsu 210023, PR China
2. Department of Earth Sciences, University College London, Gower Street, London WC1E 6BT, UK
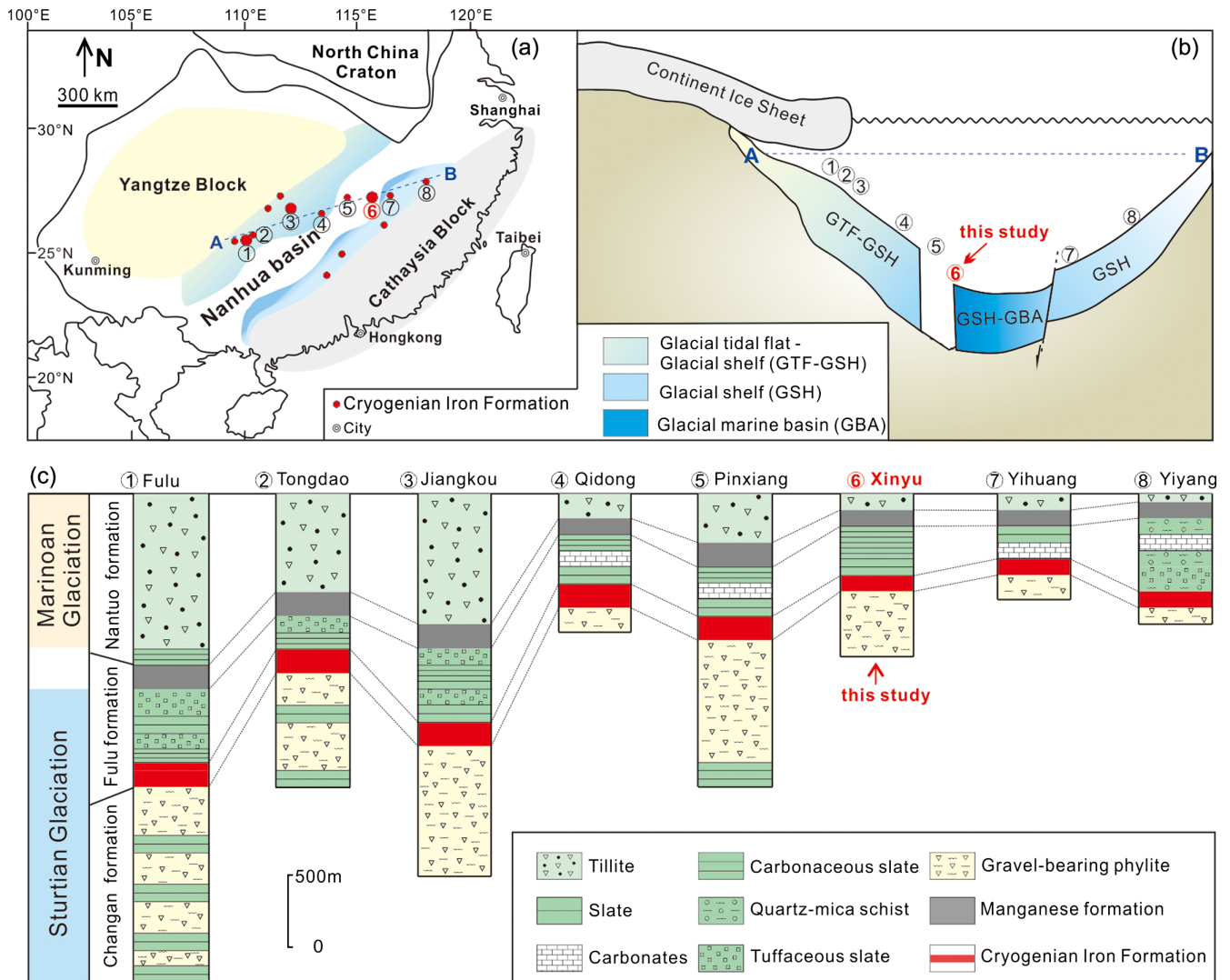* Corresponding author (email: liweiqiang@nju.edu.cn)

Figure 1 **(a)** Distribution of Cryogenian Iron Formations in South China and their tectonic setting during the Neoproterozoic. **(b)** Tectonic background and palaeo-depth of the Cryogenian iron formations, after Wang and Li (2003). **(c)** Stratigraphic correlations of different CIFs from South China, after Tang *et al.* (1987). The thickness of iron formations, manganese formations, and carbonate in between are magnified for illustration, and do not represent true thickness.

within the Nanhua rift basin that separated the Yangtze Craton and the Cathaysia Block during the Neoproterozoic Era. It was deposited in deep water (Wang and Li, 2003), and contains magnetite as the major Fe oxide mineral. The Xinyu CIF is uniform in its stratigraphic sequence and can be traced continuously for over 60 km (Fig. S-2), despite local deformation and greenschist facies metamorphism. The Xinyu CIF in the ore district is underlain by a magnetite-bearing, chlorite-sericite phyllite and overlain by a pyrite-bearing sericite phyllite (Figs. 2, S-3). The pyrite-bearing phyllite horizon is used as a faithful marker for the termination of Xinyu CIF by the local iron ore exploration geologists. Magnetite and pyrite in the sericite phyllite are generally disseminated and euhedral to subhedral in shape (Figs. S-4 to S-6). These rocks also contain platy hematite and irregular interstitial carbonates (mostly ankerite) as minor constituents (Figs. S-7, S-8). The lack of overgrowth texture in magnetite and occurrence of minute Fe oxide inclusions in ankerite suggest that the two minerals were products of early diagenesis, rather than late metamorphic events (Figs. S-9, S-10).

We characterised the Fe isotope data of magnetite and pyrite, S isotope data of pyrite, and C isotope data of interstitial carbonates from a representative drill core that intersects the strata bearing the Xinyu CIF (Fig. 2). Details of analytical methods are provided in the Supplementary Information. The $\delta^{56}Fe$ values cluster around a crustal baseline value of $+0.1$ ‰ for disseminated magnetite grains in the chlorite-sericite phyllite (Fig. 2) underlying the Xinyu CIF, but values increase monotonically up-section within the Xinyu CIF, reaching a maximum value of $+2$ ‰ at the top of the CIF. This trend is mirrored by the C isotope values of interstitial carbonates ($\delta^{13}C_{carb}$), which decrease from -7 ‰ in the lower magnetite-bearing, chlorite-sericite phyllite to -12 ‰ at the top of the Xinyu CIF. These $\delta^{13}C_{carb}$ values abruptly increase to around -8 ‰ across the boundary between CIF and the overlying sericite phyllite. This is echoed by a fundamental change in the mineralogy of the disseminated Fe-bearing minerals in the sericite phyllite, whereby magnetite changes to pyrite. The $\delta^{56}Fe$ values of the pyrite grains scatter about $+0.5$ ‰, whereas $\delta^{34}S$ values increase from a very low value of -40 ‰ to a high point of $+7$ ‰, before returning to around 0 ‰ up-section (Fig. 2).
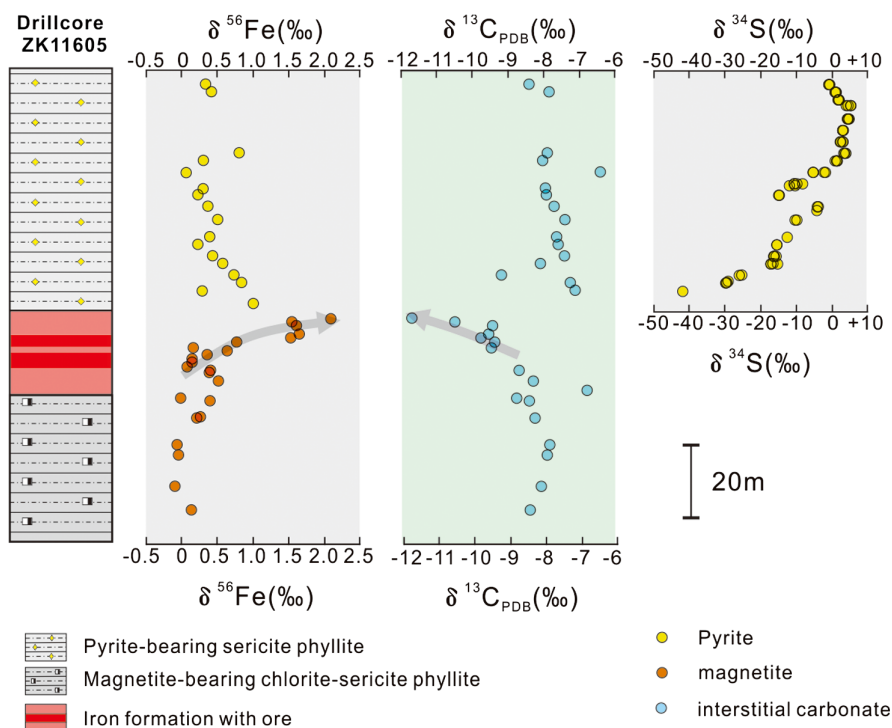
Figure 2 Stratigraphic column and Fe-C-S isotope data along a drill core of the Xinyu CIF.

Discussion

The upward trend towards higher δ^{56}Fe values within the Xinyu CIF is similar to previously reported Fe isotope patterns from Xinyu and other 'Sturtian' CIFs worldwide (Zhu *et al.*, 2019). The source of iron in the iron formations is believed to have been hydrothermal fluids that have δ^{56}Fe values close to 0 ‰ or slightly lower (Johnson *et al.*, 2008). The low δ^{56}Fe values in the lower Xinyu CIF likely record periods of efficient oxidation and quantitative removal of hydrothermal Fe(II) that occurred during the early stages of CIF deposition (Fig. 3a). Given that the primary precipitates of Fe(II) oxidation (*i.e.* Fe(III) oxides/hydroxides) enrich heavy Fe isotopes over aqueous Fe(II) by ~3–4 ‰ at equilibrium (Johnson *et al.*, 2008), the positive δ^{56}Fe values in iron formations are most parsimoniously explained by partial oxidation of hydrothermal Fe(II) (Johnson *et al.*, 2008; Li *et al.*, 2013). Increasing δ^{56}Fe up-section in the CIFs, therefore, reflects a decreasing availability of free O_2 to oxidise Fe(II)$_{aq}$ in the Cryogenian oceans (Fig. 3b). Decreased O_2 production seems unlikely in deglacial oceans, as removal of ice sheets would have allowed photosynthetic organisms to thrive, and moreover, newly resumed global hydrological cycles would have delivered abundant nutrient elements (*e.g.*, P) into the oceans to boost biological productivity (Shields *et al.*, 1997; Och and Shields-Zhou, 2012). Therefore, development of a redoxcline and decrease in oxidation efficiency (*i.e.* increase in partial oxidation) of deep water Fe(II) seems a more plausible explanation for the Fe isotope trend recorded in the Xinyu CIF (Fig. 3b).

Concomitant with the up-section increase in magnetite δ^{56}Fe, there is a decrease in δ^{13}C$_{carb}$ from mantle-like values of around −8 ‰ in the sericite phyllite to values as low as −12 ‰ at the top of the Xinyu CIF. Low δ^{13}C$_{carb}$ values in carbonates frequently reflect contributions from organic C that has significantly lower δ^{13}C values than dissolved inorganic carbon. Dissimilatory iron reduction (DIR) by microbes in soft sediments has been identified as an effective mechanism that transforms

Fe(III) hydroxides into magnetite and remineralises organic carbon to form low δ^{13}C diagenetic carbonates (Heimann *et al.*, 2010; Craddock and Dauphas, 2011). The decreasing δ^{13}C$_{carb}$ values within the Xinyu CIF could therefore reflect increasing delivery to the seafloor of organic matter and efficient remineralisation by DIR microbes. The activity of O_2-respiring heterotrophic microbes in the water column in the presence of abundant organic matter supply would consume dissolved O_2, producing mid-column anoxia, which lowered the intensity of aqueous Fe(II) oxidation, producing high δ^{56}Fe Fe(III) precipitates (Fig. 3b). Therefore, the C isotope record corroborates the Fe isotope evidence for a strengthening of redox stratification during precipitation of the upper part of the Xinyu CIF.

The termination of CIF deposition at Xinyu was immediately followed by deposition of rocks containing pyrite with very low (−40 ‰) δ^{34}S values (Fig. 2). Deposition of pyrite requires S^{2-}, which could be provided by microbial reduction of SO_4^{2-} in the presence of organic matter. It is widely accepted that sulfate was depleted in oceans during the Snowball Earth Events (Kump and Seyfried, 2005). Deglaciation, however, could have provided a source of sulfate *via* renewed riverine input from continents. The dissolved sulfate was delivered to oceans by rivers, but due to density differences, the sulfate likely spread initially within plumes of freshwater at the surface mixing zone, separated from the organic-rich water body and seafloor below the redoxcline (Fig. 3b). As soon as sulfate could reach beneath the redoxcline, microbes would have been capable of metabolising organic matter *via* the bacterial sulfate reduction pathway, releasing H_2S that reacted with hydrothermal Fe^{2+} to form low solubility Fe sulfide precipitates (Fig. 3c). Predominance of bacterial sulfate reduction therefore terminated the deposition of Fe(III) hydroxides in CIF.

The pyrite grains that precipitated immediately after the CIF have very low (−40 ‰) δ^{34}S values. Experiments have shown that the magnitude of S isotope fractionation associated with bacterial sulfate reduction is controlled by the amount of sulfate, whereby the maximum Δ^{34}S$_{sulfate-sulfide}$ fractionation
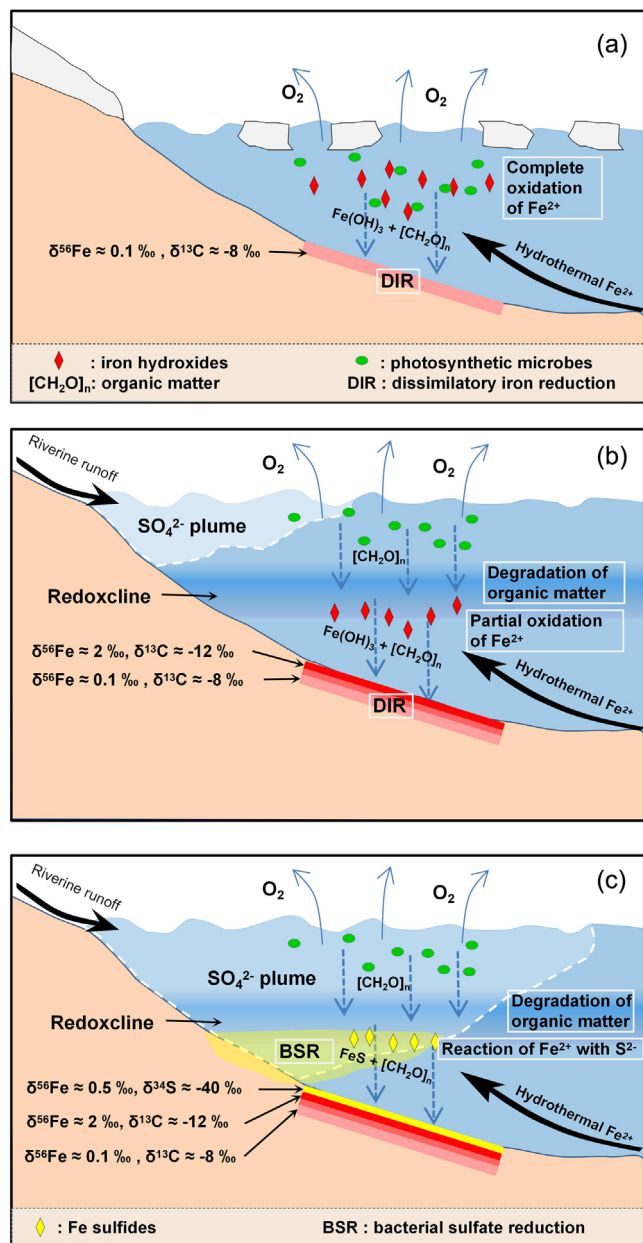
Figure 3 A conceptual model for initiation, development, and termination of Cryogenian iron formations.

factor of ~45 ‰ occurs in the presence of >1 mM sulfate in water (Habicht and Canfield, 1997). Therefore, the very low $\delta^{34}S$ signatures of pyrite require that bacterial sulfate reduction started with abundant (>1 mM) dissolved sulfate. The onset of pyrite precipitation after CIF termination implies a rapid delivery of abundant sulfate to deeper oceans. The increase in pyrite $\delta^{34}S$ values implies that the consumption of dissolved sulfate by bacterial sulfate reduction outpaced replenishment of sulfate from rivers, leading to a decrease in the global ocean sulfate reservoir, and progressively higher $\delta^{34}S$ in residual sulfate.

The Fe-C-S isotope record presents a compelling case for termination of CIF deposition by sulfur cycling and extensive development of euxinia in the water column of deglacial Cryogenian oceans. It has been proposed that the termination of major banded iron formations around 1.8 Ga was caused by the development of euxinic oceans (Poulton et al., 2004). Deposition of pyrite-bearing sediments following ironstone deposition has not been reported from CIF sequences in other

parts of the world, so it is possible that the Xinyu CIF is a special case that is different from other CIFs in terms of the pathway of IF termination. This can be explained by the differences in the depth of IF deposition. Xinyu CIF was deposited in a deep marine setting based on sedimentary facies analysis (Tang et al., 1987) and palaeogeographic reconstruction (Wang and Li, 2003), therefore the spread of ocean euxinia is recorded by the deep Xinyu CIF, but not in other shallow CIFs as Fe(II) delivery was cut in deeper seawater. A recent study reported widespread euxinia at the end of Marinoan glaciation, whereby the abundance of pyrite nodules was significantly greater in deep settings than in shallow settings (Lang et al., 2018). We therefore argue that the spread of euxinia into deep oceans and titration of hydrothermal Fe^{2+} by sulfides is a viable mechanism to explain the disappearance of IFs after the Cryogenian Period. If so, the mineralogical and isotopic records of the Xinyu CIF pinpoint the onset of euxinia, which was to be become widespread along productive margins until the Cambrian (Li et al., 2010). Isotopic records from the Xinyu CIF also testify to the diversity and prosperity of the ocean microbial community. A microbial ecosystem of diverse metabolisms, including oxygenic photosynthesis, O_2-respiring heterotrophism, DIR, and BSR thrived through cycling of redox elements (O-C-S-Fe) in Cryogenian oceans upon deglaciation.

Acknowledgements

Additional Information

Supplementary Information accompanies this letter at http://www.geochemicalperspectivesletters.org/article2025.

References

CANFIELD, D.E. (1998) A new model for Proterozoic ocean chemistry. *Nature* 396, 450–453.

CANFIELD, D.E., POULTON, S.W., KNOLL, A.H., NARBONNE, G.M., ROSS, G., GOLDBERG, T., STRAUSS, H. (2008) Ferruginous Conditions Dominated Later Neoproterozoic Deep-Water Chemistry. *Science* 321, 949.

CANFIELD, D.E., ZHANG, S., WANG, H., WANG, X., ZHAO, W., SU, J., BJERRUM, C.J., HAXEN, E.R., and HAMMARLUND, E.U., HAMMARLUND, E.U. (2018) A Mesoproterozoic iron formation. *Proceedings of the National Academy of Sciences* 115, E3895.

COX, G.M., HALVERSON, G.P., MINARIK, W.G., LE HERON, D.P., MACDONALD, F.A., BELLEFROID, E.J., STRAUSS, J.V. (2013) Neoproterozoic iron formation: An evaluation of its temporal, environmental and tectonic significance. *Chemical Geology* 362, 232–249.

CRADDOCK, P.R., DAUPHAS, N. (2011) Iron and carbon isotope evidence for microbial iron respiration throughout the Archean. *Earth and Planetary Science Letters* 303, 121–132.

GUILBAUD, R., POULTON, S.W., BUTTERFIELD, N.J., ZHU, M., SHIELDS-ZHOU, G.A. (2015) A global transition to ferruginous conditions in the early Neoproterozoic oceans. *Nature Geoscience* 8, 466–470.

HABICHT, K.S., CANFIELD, D.E. (1997) Sulfur isotope fractionation during bacterial sulfate reduction in organic-rich sediments. *Geochimica et Cosmochimica Acta* 61, 5351–5361.

HEIMANN, A., JOHNSON, C.M., BEARD, B.L., VALLEY, J.W., RODEN, E.E., SPICUZZA, M.J., BEUKES, N.J. (2010) Fe, C, and O isotope compositions of banded iron formation carbonates demonstrate a major role for dissimilatory iron reduction in ~2.5 Ga marine environments. *Earth and Planetary Science Letters* 294, 8–18.

HOFFMAN, P.F., SCHRAG, D.P. (2002) The snowball Earth hypothesis: testing the limits of global change. *Terra Nova* 14, 129–155.

HOFFMAN, P.F., ABBOT, D.S., ASHKENAZY, Y., BENN, D.I., BROCKS, J.J., COHEN, P.A., COX, G.M., CREVELING, J.R., DONNADIEU, Y., ERWIN, D.H., *et al.* (2017) Snowball Earth climate dynamics and Cryogenian geology-geobiology. *Science Advances* 3, e1600983.

JOHNSON, C.M., BEARD, B.L., RODEN, E.E. (2008) The Iron Isotope Fingerprints of Redox and Biogeochemical Cycling in Modern and Ancient Earth. *Annual Review of Earth and Planetary Sciences* 36, 457–493.

KIRSCHVINK, J.L. (1992) Late Proterozoic low-latitude global glaciation: The snowball Earth. In: SCHOPF, J.W., KLEIN, C. (Eds.) Cambridge University Press, Cambridge.

KUMP, L.R., SEYFRIED, W.E. (2005) Hydrothermal Fe fluxes during the Precambrian: Effect of low oceanic sulfate concentrations and low hydrostatic pressure on the composition of black smokers. *Earth and Planetary Science Letters* 235, 654–662.

LANG, X., SHEN, B., PENG, Y., XIAO, S., ZHOU, C., BAO, H., KAUFMAN, A.J., HUANG, K., CROCKFORD, P. W., LIU, Y., *et al.*, (2018) Transient marine euxinia at the end of the terminal Cryogenian glaciation. *Nature Communications* 9, 3019.

LI, C., LOVE, G.D., LYONS, T.W., FIKE, D.A., SESSIONS, A.L., CHU, X. (2010) A Stratified Redox Model for the Ediacaran Ocean. *Science* 328, 80.

LI, W., CZAJA, A.D., VAN KRANENDONK, M.J., BEARD, B.L., RODEN, E.E., JOHNSON, C.M. (2013) An anoxic, Fe(II)-rich, U-poor ocean 3.46 billion years ago. *Geochimica et Cosmochimica Acta* 120, 65–79.

OCH, L.M., SHIELDS-ZHOU, G.A. (2012) The Neoproterozoic oxygenation event: Environmental perturbations and biogeochemical cycling. *Earth-Science Reviews* 110, 26–57.

POULTON, S.W., FRALICK, P.W., CANFIELD, D.E. (2004) The transition to a sulphidic ocean ~1.84 billion years ago. *Nature* 431, 173–177.

SAHOO, S.K., PLANAVSKY, N.J., KENDALL, B., WANG, X., SHI, X., SCOTT, C, ANBAR, A.D., LYONS, T.W., JIANG, G. (2012) Ocean oxygenation in the wake of the Marinoan glaciation. *Nature* 489, 546–549.

SHIELDS, G., STILLE, P., BRASIER, M.D., ATUDOREI, N. (1997) Stratified oceans and oxygenation of the late Precambrian environment: a post glacial geochemical record from the Neoproterozoic of W. Mongolia. *Terra Nova* 9, 218–222.

SHIELDS, G.A., MILLS, B.J.W., ZHU, M., RAUB, T.D., DAINES, S.J., LENTON, T.M. (2019) Unique Neoproterozoic carbon isotope excursions sustained by coupled evaporite dissolution and pyrite burial. *Nature Geoscience* 12, 823–827.

TANG, J., FU, H., YU, Z. (1987) Stratigraphy, type and formation conditions of the late precambrian banded iron ores in south China. *Chinese Journal of Geochemistry* 6, 331–341.

WANG, J., LI, Z. (2003) History of Neoproterozoic rift basins in South China: implications for Rodinia break-up. *Precambrian Research* 122, 141–158.

ZHU, X., SUN, J., LI, Z. (2019) Iron isotopic variations of the Cryogenian banded iron formations: A new model. *Precambrian Research* 331, 105359.

Termination of Cryogenian ironstone deposition by deep ocean euxinia

C. Wu, T. Yang, G.A. Shields, X. Bian, B. Gao, H. Ye, W. Li

Supplementary Information

The Supplementary Information includes:

- ➢ 1. Geological Background of the Xinyu Iron Formation
- ➢ 2. Petrography and Mineral Chemistry of the Xinyu Iron Formation
- ➢ 3. Analytical Methods and Data Tables
- ➢ Figures S-1 to S-10
- ➢ Tables S-1 to S-3
- ➢ Supplementary Information References

1. Geological Setting, Regional Geology and Stratigraphy

The South China Block consists of the Yangtze Block and the Cathaysia Block (Zhao and Cawood, 2012). These two blocks collided between the Late Mesoproterozoic to the earliest Neoproterozoic (Wang and Li, 2003; Wang *et al.*, 2014), leading to the formation of the ~1500km Jiangnan orogen (Wang *et al.*, 2014). Meso-Neoproterozoic sedimentary sequences widely developed around the Yangtze Block and along the northwestern Cathaysia Block, and consist of two main parts that are separated by a regional unconformity (Fig. S-1; Wang and Li., 2003; Wang *et al.*, 2012).
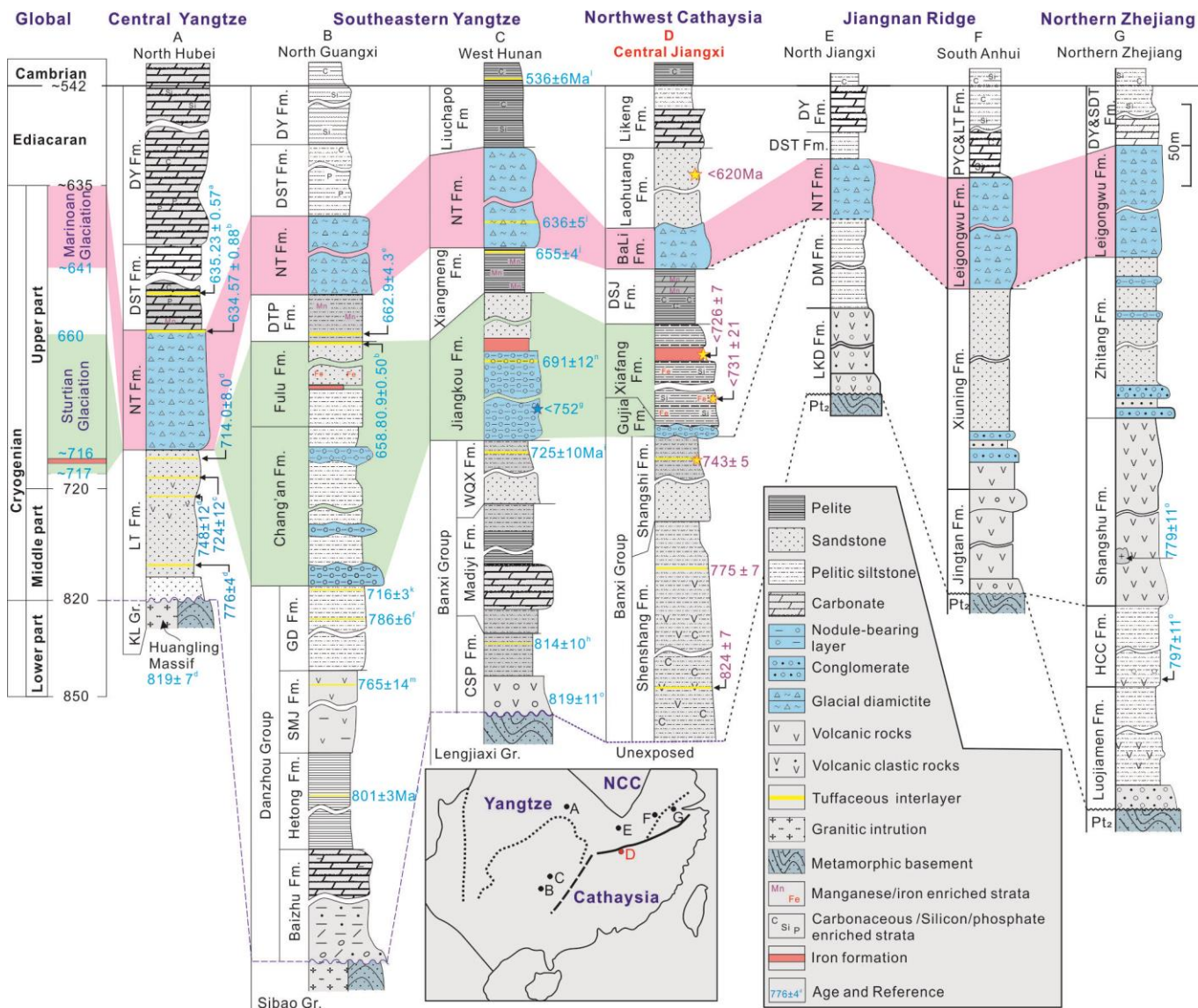
Figure S-1 Correlation of representative Neoproterozoic strata in South China (modified from Wang and Li, 2003; Yang *et al.*, 2012). NCC-North China Craton; WQX Fm.-Wuqiangxi formation; SMJ Fm.-Sanmengjie formation; CSP Fm.-Cangshuipu formation; GD Fm.-Gongdong formation; XM Fm.-Xiangmeng formation; DTP Fm.- Datangpo formation. KL Gr.-Kongling Group; NT Fm.-Nantuo formation; DST Fm.-Doushantuo formation; DY Fm.-Denying formation; LKD Fm.-Luokedong formation; DM Fm.-Dongmen formation; LGW Fm.-Leigongwu formation; PYC&LT Fm.-Piyuancun&Lantian formation; DY&DST Fm.-Dengying&Doushantuo formation; HCC Fm.- Hongchicun formation; Ages of the first column are from Rooney *et al.* (2015) and references therein, while ages of the column of Central Jiangxi are from this study. a-Condon *et al.*, 2005; b-Zhou *et al.*, 2019; c-Lan *et al.*, 2015a; e-Zhou *et al.*, 2004; c-Ma *et al.*, 1984; d-Lan *et al.*, 2015b; e-Zhou *et al.*, 2004; f-Gao *et al.*, 2013; g-Wang *et al.*, 2012; h-Gao et a., 2014; i-Zhang *et al.*, 2008; j-Zhang *et al.*, 2008; k-Lan *et al.*, 2014; Chen *et al.*, 2009; m-Zhou *et al.*, 2007; m-Lan *et al.*, 2015a; o-Li *et al.*, 2003.

The lower sedimentary sequence below the unconformity is named as the Sibao Group in northern Guangxi province, the Lengjiaxi Group in Hunan province, the Fanjingshan Group in Guizhou province, the Shuangxiwu Group in Zhejiang province, and the Shuangqiaoshan Group in Jiangxi province (Wang and Li., 2003), representing the collision between the Yangtze Block and the Cathaysia Block (Wang *et al.*, 2014). The upper sedimentary sequence above the unconformity consists of sedimentary rocks produced by the Nanhua rifting system that developed at the suture zone between the Yangtze Block and the Cathaysia Block (Fig.S-1).

The Nanhua rifting Basin, from bottom to top, consists of the lower pre-Cryogenian siliciclastic units, the middle Cryogenian glacial and non-glacial deposits and the upper Ediacaran carbonate–siliciclastic rocks (Jiang *et al.*, 2003). The Cryogenian strata in Nanhua rifting basin can be divided into the lower glacial diamictite (the Chang'an/Jiangkou formations and their correlative equivalents), the middle non-glacial shale and siltstone units (the Datangpo Formation and its equivalents), and the upper glacial diamictite (the Nantuo Formation) (Jiang *et al.*, 2003; Zhou *et al.*, 2004; Jiang *et al.*, 2011; Bao *et al.*, 2018). The Chang'an/Jiangkou formations and their correlative equivalents are commonly correlated with the Sturtian glaciation, whereas the Nantuo Formation is correlated with the Marinoan glaciation (e.g., Hoffman and Li, 2009). A number of Neoproterozoic iron formations (IFs) develop in the Nanhua rifting basin (e.g., Fulu and Xinyu IF) (Fig. 1a,c) (Tang, 1987). The Fulu IF was deposited in the shallow-water conditions, whereas the Xinyu BIF was deposited in deep-water settings (Fig. 1a,b) according to its sentimentology characters (Wang and Li, 2003).
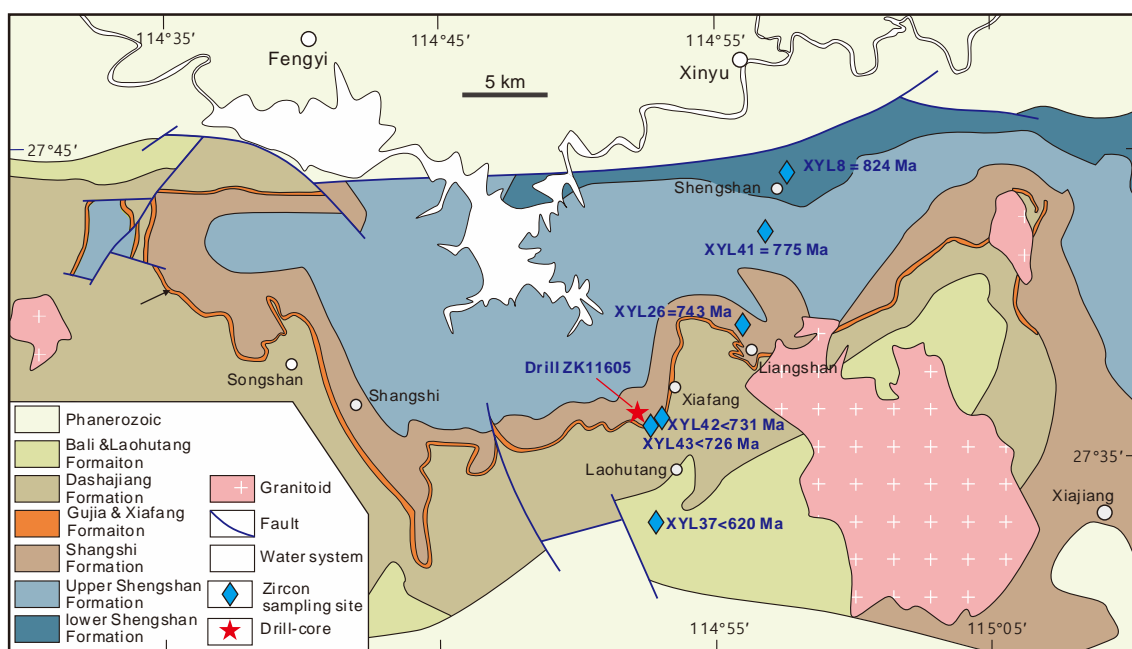
Figure S-2 Geological map of the Xinyu iron formation (Modified from Meng *et al.*, 2017).

Neoproterozoic iron formations from South China exhibit features that are similar to those from eastern Australia and western Laurentia (Eisbacher, 1985; Jiang *et al.*, 2006; Busigny *et al.*, 2018). Major rifting during the late mid-Proterozoic to early Neoproterozoic set the tectonic background for deposition of many of the Neoproterozoic IFs (Fig. 1). The Xinyu Iron Formation was deposited in the central zone of the Nanhua Rift Basin (Fig. 1), underlain by Gujia Formation with pebble-bearing sandy slate and diamictite, with the overlying Dashajiang Formation and Bali Formation (Fig.S-1, Tang *et al.* 1987; Yang *et al.*, 2012).
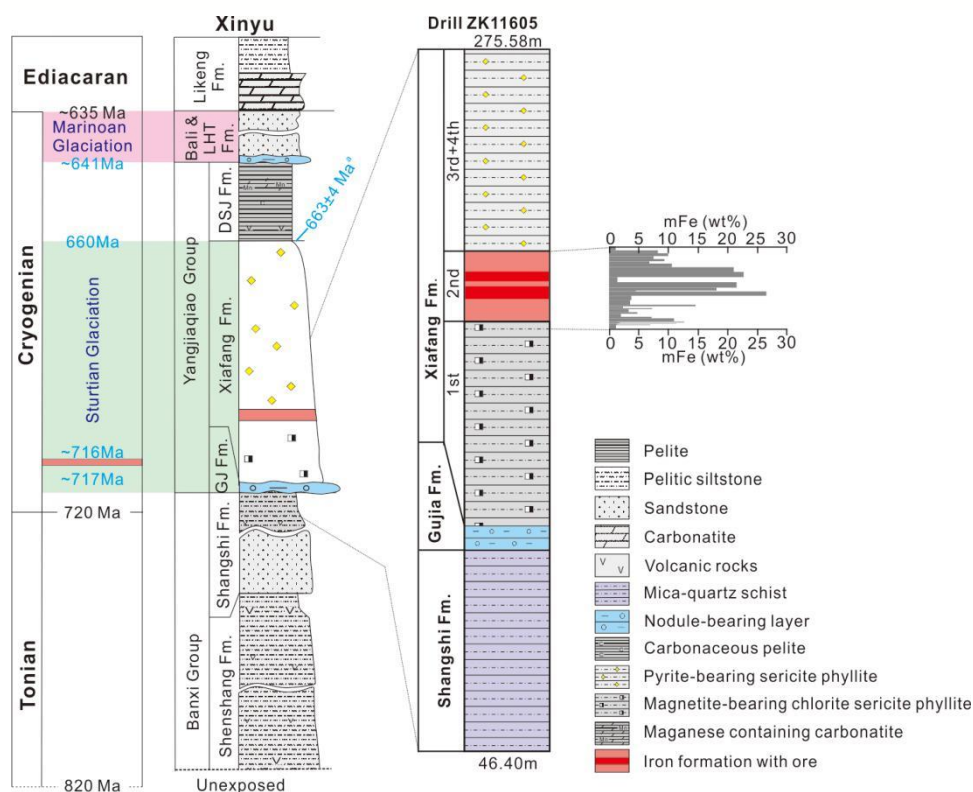
Figure S-3 Variation in lithology and iron content of Xinyu CIF along the drill core ZK11605.

The Sinian system, which contains the Xinyu IF (Fig. S-2), is made up of four unconformity-bounded sequences, that is, the Shengshan formation, the Shangshi formation, the Gujia formation, the Xiafang formation, the Dashajiang formation, the Bali formation, the Laohutang formation and the Likeng formation (Tang *et al.*, 1987, Fig. S-3). The Shengshan formation is mainly sericite phyllite interbedded by several layers of volcanic rocks, while the Shangshi formation is mainly quartz mica schist with some phyllitic sandstone. Both the shengshan and Shangshi formation composed the Banxi group in Central Jiangxi and West Hunan, which is equivalent to the Danzhou Group in North Guanxi and the Xiajiang Group in South Guizhou (Fig. S-1, Song *et al.*, 2017 and references therein). The Yangjiaqiao Group is composed by the lower conglomeratic formation (Gujia Foramtion), the middle ironstone–bearing Xiafang Formation, and the upper manganese-containing Dashajiang Formation (Fig. S3, Yao *et al.*, 1993). The Gujia Formation from the Xinyu area is only several meters thick, and contains magnetite-bearing chlorite sericite phyllite and carbonaceous pseudo-conglomerate. Tang (1987) interpreted the Gujia Formation as an interglacial to glacial deposits Sturtian in age, which is equivalent to the Chang'an formation in North Guangxi and the lower Jiangkou formation in West Hunan (Fig. S-1), correlative with the widespread late Precambrian diamictite strata in South China (Fig. 1c). Contained the Xinyu iron formation, the Xiafang formation is mainly phyllite, which is correlative with the Fulu formation in North Guanxi and the upper Jiangkou formation in West Hunan (Fig. S-1). The Dashajiang Formation contains gravel-containing sericite phyllite with carbon-bearing sericite phyllite, chlorite phyllite, meta-sandstone and manganese carbonate, correlative with the widespread manganese strata of the Datangpo formation in North Guangxi, the Xiangmeng formation in West Hunan (Fig. S-1), which is identified as the interglacial interval between the Sturtian and the Marinoan glaciation (Fig. S-1, Tang *et al.* 1987; Yang *et al.*, 2012).

2. Petrographic and mineralogical features of the Xinyu IF

The Shangshi formation consists of chlorite-sericite phyllite. Widely disseminated magnetite and carbonate occur together with quartz lens that are conformable with oriented muscovite (Fig. S-4a). The Gujia Formation contains magnetite-bearing chlorite sericite phyllite and carbonaceous pseudo-conglomerate (Fig. S-4b). Most carbonaceous pseudo-conglomerate in the formation are ellipsoidal or subrounded in shape, and distribute conformably with their host-sequence (Fig. S-4b).
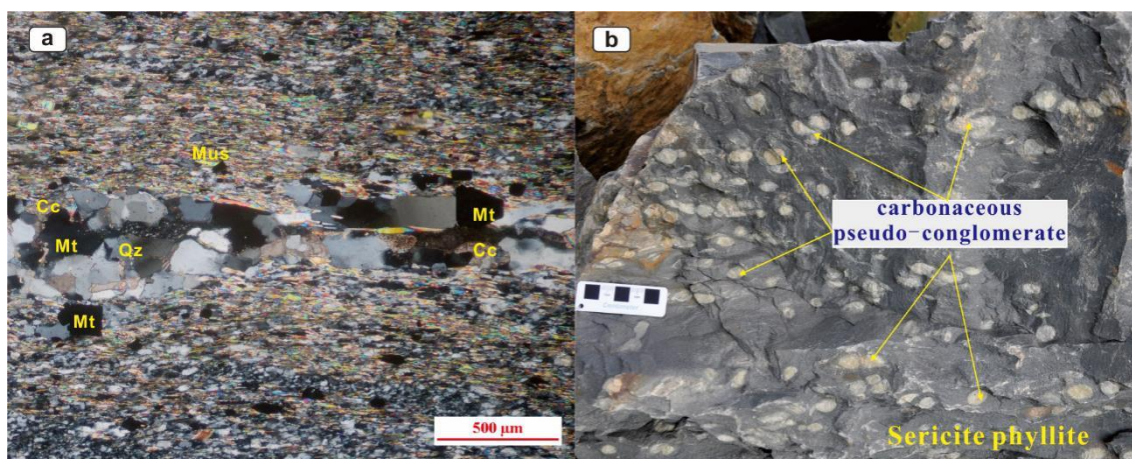
Figure S-4 (a) Microphotograph of the chlorite-sericite phyllite of Shangshi Formation from drill core ZK11605 (cross polarization). **(b)** Photo of Carbonaceous pseudo-conglomerate in magnetite-bearing chlorite sericite phyllite of Gujia Formation. Qz-quartz; Mt- magnetite; Cc-carbonate; Py-pyrite; Ms-muscovite

The Xiafang Formation is composed of three members, which are, stratigraphically upsection, the 1st member that contains magnetite-bearing chlorite sericite phyllite, the 2nd member that is the Xinyu iron formation, and the 3rd member that contains pyrite -bearing chlorite sericite phyllite. The petrographic features of the 1st member are similar to those of the Shangshi formation, that disseminated magnetite grains occur in both quartz veins and the sericite-chlorite matrix, together with interstitial carbonate. The 3rd member is also a chlorite sericite phyllite that share petrographic similarities with the 1st member, except that the iron-bearing mineral is pyrite, instead of magnetite.
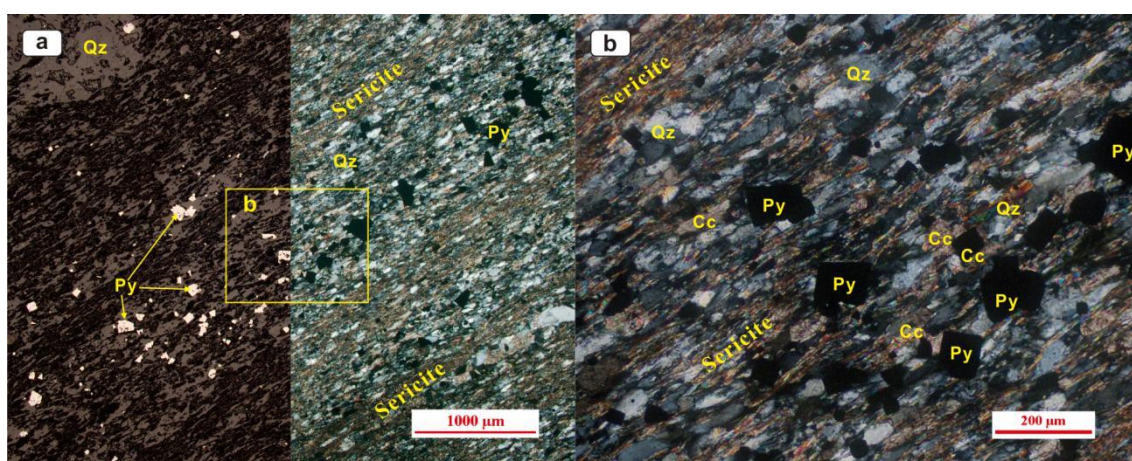
Figure S-5 Microphotographs of the pyrite-bearing sericite phyllite of Xiafang Formation (Left image in plane reflected light).

Quartz and magnetite are the two major constituents for the 2nd member of the Xiafang Formation, the Xinyu iron formation, accounting for more than 90% in volume (Fig. S-6a). The contents of magnetite vary from ca. 5% up to ca. 40% in volume. Beside quartz and magnetite, calcite is also an abundant mineral in the iron formation, while muscovite and chlorite could be found under microscope (Fig. S-6b).

In addition to magnetite, hematite occurs as a minor Fe-oxide phase in some iron formation samples. The hematite grains are generally platy in shape, and display preferred orientation that is conformable with sedimentary beddings, indicating the early diagenetic origin of the hematite. Replacement of hematite by magnetite can be identified in some cases, implying that at least some magnetite grains were produced later than the hematite grains. (Fig. S-6c, d).
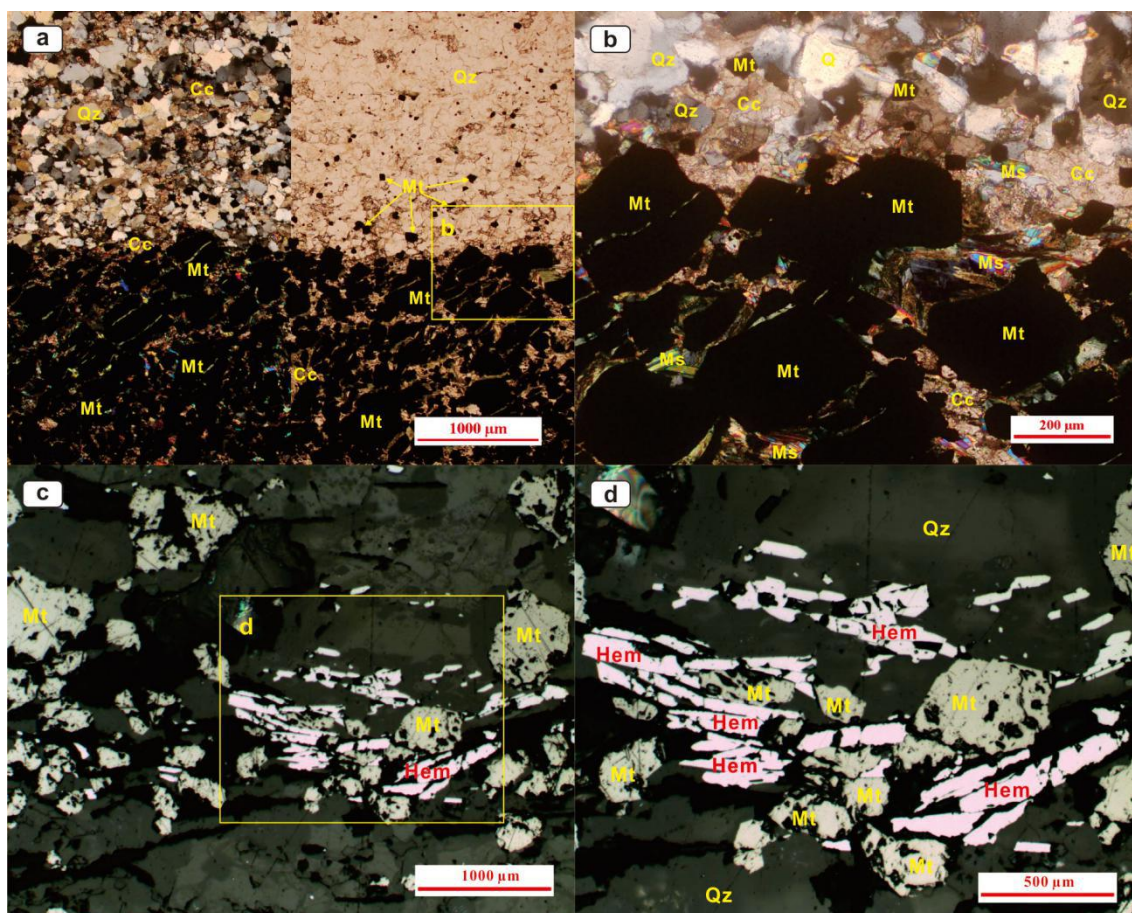
Figure S-6 Photo micrographs of the ironstone from the second member of Xiafang Formation, showing quartz and magnetite-rich bands in **a**, showing characters of quartz, magnetite, carbonates and muscovite in **b**. a-Quartz and magnetite-rich bands in iron formation.b-Zone-in of square in Fig. S-6a, showing characters of quartz, magnetite, calcite and muscovite. **c**-Platy hematite and granular magnetite grains display orientation with sedimentary beddings. **d**-Granular magnetite grain replaces hematite in iron formation band.

Intergrowth of magnetite and carbonates is a common feature in Xinyu iron formation (Fig. S-7). The majority of the interstitial carbonates are ankerite , and a minor proportion of the carbonates are calcite (Fig. S-8).
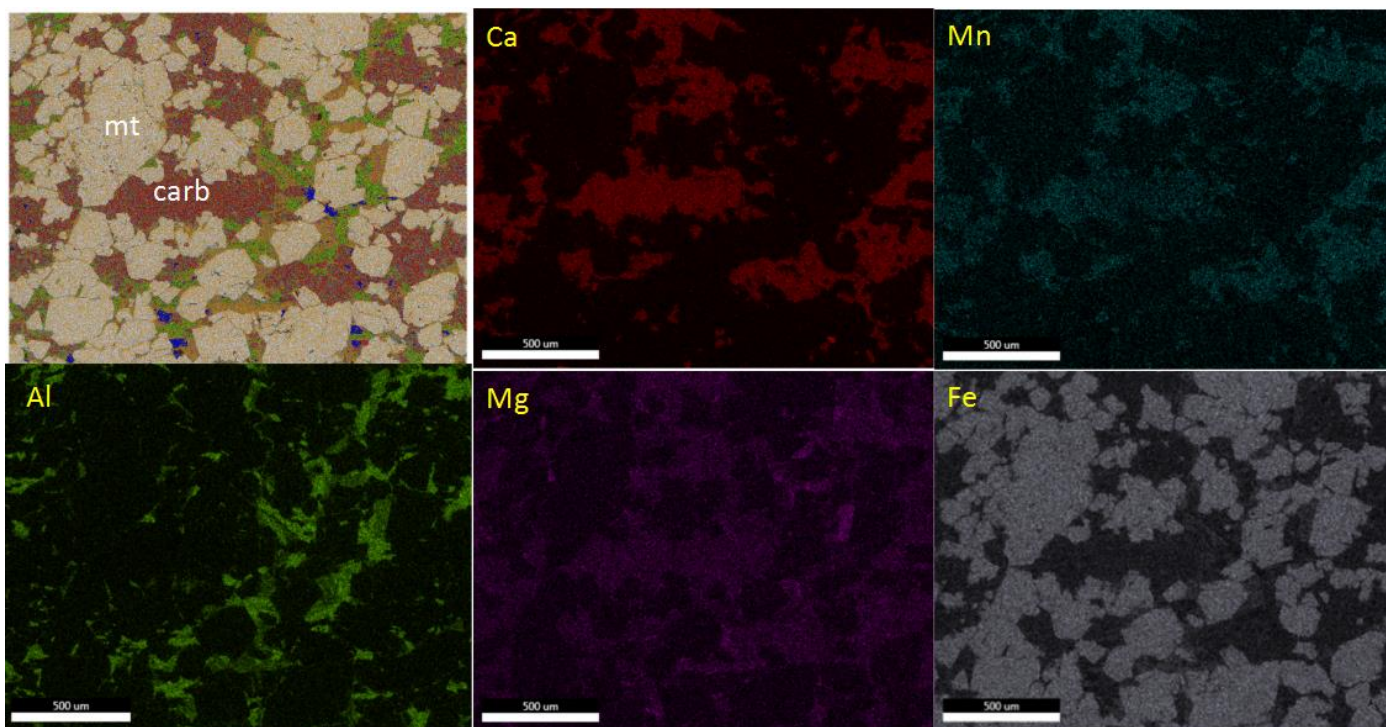
Figure S-7 Elemental mapping (EDS-SEM) of a representative IF sample, which shows intergrowth of magnetite with siderite that contains Ca, Mn, Mg, and Fe.
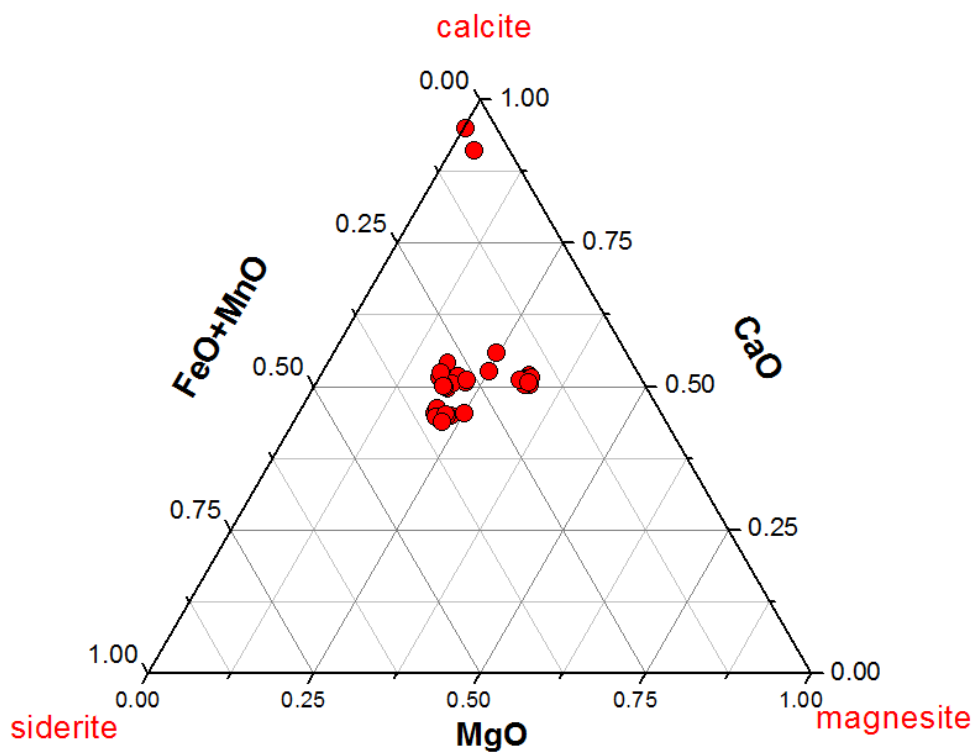
Figure S-8 Tertiary plot of the mineral chemistry of carbonates in samples from drill core ZK11605.

2.1. Evidence of diagenetic origin for the magnetite grains from the Xinyu IF
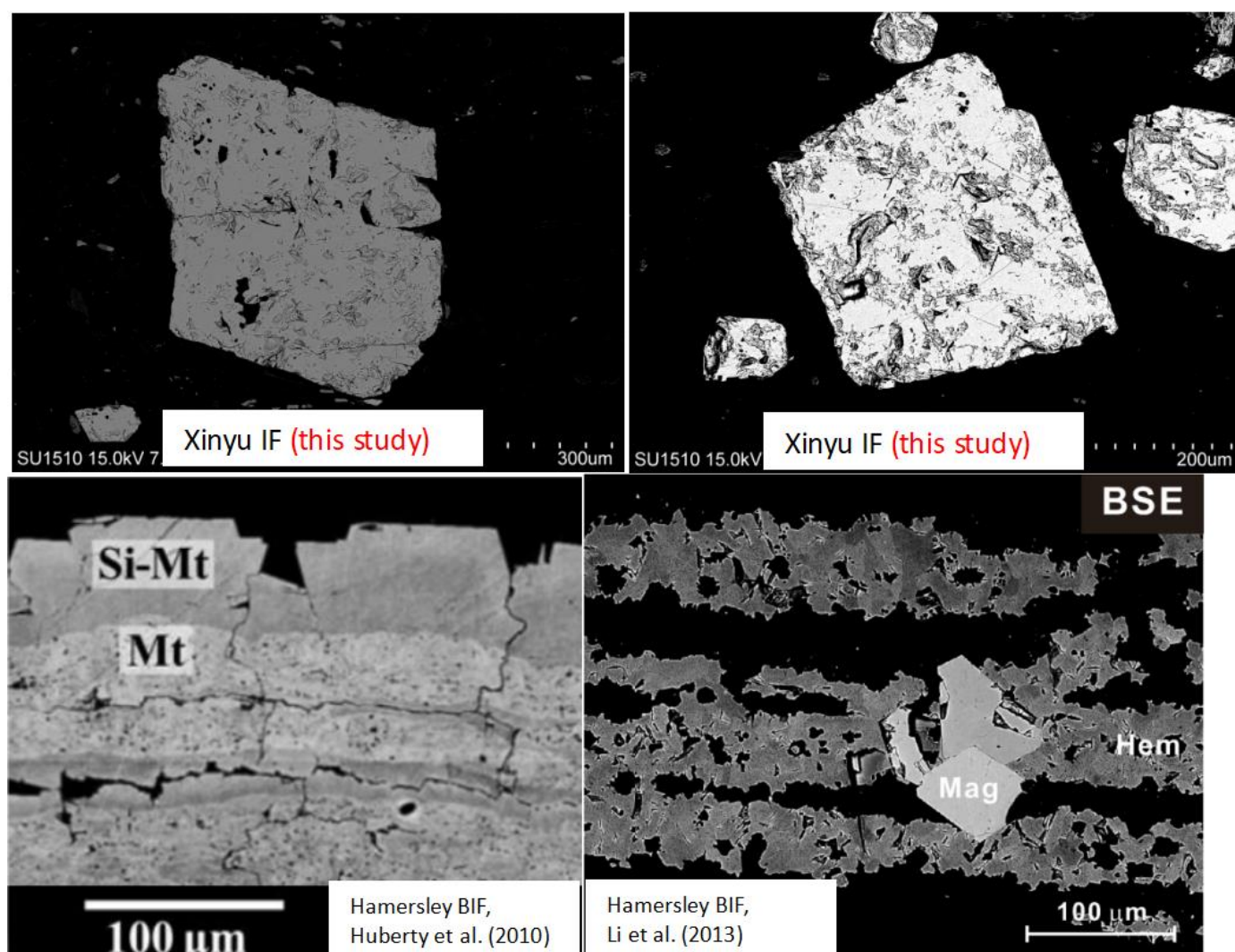
Figure S-9 Comparison of magnetite from Xinyu iron formation (upper two figures), with magnetite from Hamersley banded iron formation in literature (lower two figures). All images were taken using SEM under backscattering model with the highest possible contrast to resolve possible zoning in magnetite.

The magnetite grains from Xinyu IF typically contain numerous microscopic mineral inclusions, and in many cases the apparent large and euhedral magnetite crystals are product of attachment of small crystals. They do not show morphological characteristics of magnetite of metamorphic/hydrothermal origin, which typically lacks mineral inclusions, and show true euhedral crystal habits.

Huberty *et al.* (Huberty *et al.*, 2012) and (Li *et al.*, 2013) showed that metamorphic magnetite in band iron formations are typically silician magnetite, and can form characteristic core-ring textures under backscatter imaging mode under scanning microscope. Fe and O isotope data indicate that the low-Si magnetite cores are of diagenetic origin. Such diagenetic magnetite contains abundant mineral inclusions (see left figure above). By contrast, the silician magnetite form rings on the low-Si magnetite cores or individual crystals are euhedral in shape and clear, lacking mineral inclusions. The core-ring texture is lacking in magnetite grains from the Xinyu IF, indicating that the magnetite in Xinyu IF is not metamorphic in origin.

2.2. Evidence of diagenetic origin for interstitial ankerite from the Xinyu IF
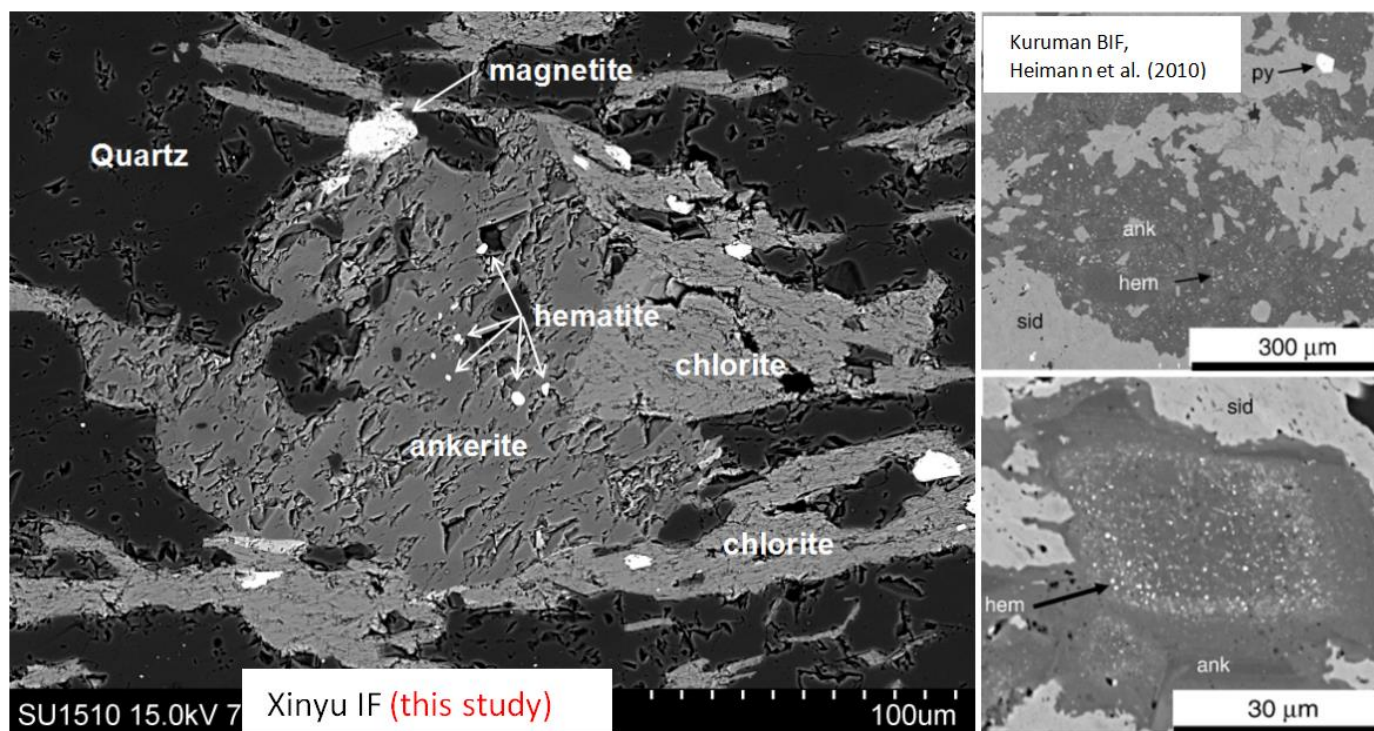
Figure S-10 Comparison of ankerite from Xinyu iron formation (left figures), with ankerite from the Hamersley banded iron formation (two smaller figures in right).

Interstitial carbonates are common in the sedimentary sequence of Xinyu. In the ironstones, interstitial carbonates are mostly ankerite. The ankerite commonly contains disseminated, micro-size hematite inclusions. Such texture has been reported by (Heimann *et al.*, 2010) from the 2.5 Ga Kuruman banded iron formation where ankerite is rigorously proven as early diagenetic via an dissimilatory iron reduction pathway by combined Fe and C isotopes. The hematite mineral inclusions within ankerite are interpreted as remnant of Fe-oxyhydroxide precipitates in soft sediment that was not transformed to ankerite in incomplete dissimilatory iron reduction. Such texture cannot be produced by hydrothermal activity, and has not been reported in literature on hydrothermal ankerite.

3. Analytical Methods and Data Tables

3.1 Iron isotope analysis

Based on petrographic observation, pyrite and magnetite grains were sampled from the drill core chips using a hand-hold microdrill with a tungsten carbide drill bit. Approximately 10mg of the mineral powder for each sample was dissolved and Fe was separated from matrix elements by anion exchange chromatography that followed an established protocol (Du *et al.*, 2017). Recovery of Fe was monitored for every sample by ICP-OES and was always >95% and the total procedural blank of the chemistry was negligible relative to the mass of Fe processed.

Iron isotope ratios were measured using a Thermo Fisher Scientific Neptune Plus MC-ICP-MS at State Key Laboratory for Mineral Deposit Research, Nanjing University. Details about the mass spectrometry has been documented in (Du *et al.*, 2017). Iron isotope compositions are reported as $\delta^{56}Fe$ relative to the international standard of IRMM-014: $\delta^{56}Fe_{sample} = [(^{56}Fe / {}^{54}Fe)_{sample} / (^{56}Fe / {}^{54}Fe)_{IRMM-014} - 1] \times 1000$ [‰]. The typical internal precision (2standard error or 2SE) was better than ±0.03‰ for $^{56}Fe/^{54}Fe$ and ±0.05‰ for $^{57}Fe/^{54}Fe$. The long-term external reproducibility (2 standard deviation or 2SD) of Fe isotope analysis is better than ±0.06‰ in $^{56}Fe/^{54}Fe$ and ±0.16‰ in $^{57}Fe/^{54}Fe$, based on repeat analysis of multiple Fe isotope standard solutions against in-house stock solutions. Accuracy of Fe isotope measurements was confirmed by repeated measurements of reference samples and USGS rock standards that were treated as unknowns with the IF samples. $\delta^{56}Fe$ of these standards are all consistent with the recommended values in literature within analytical uncertainty (Table S-1).

3.2 Carbon isotope analysis

Approximately 2-10 mg of rock powder was scrapped off the drill core chips from areas where pyrite and magnetite grains were drilled, and was placed in a cleaned and dried quartz tube that was tightly capped with a rubber stopper, and was purged with N_2 before injection of ~ 3 ml of concentrated H_3PO_4 ("104 %"). The tube was thermally equilibrated on an automated heating bench at 70 °C, then reacted for > 36 hours. Carbon isotope compositions were determined using a Finnigan Delta Plus XP continuous flow isotope ratio mass spectrometer in the stable isotope laboratory at Nanjing University. Carbon isotope data are reported using standard δ notation as $\delta^{13}C$ values, using the PDB scales, respectively. All isotope ratios were normalized to the V-PDB standard and reported in per mil (‰). Internal analytical error (2 standard error or 2SE) is less than 0.03‰ for $\delta^{13}C$. External reproducibility was checked by repeat analysis of different in-house carbonate standards and was better than ±0.5‰ for $\delta^{13}C$.

3.3 Sulfur isotope analysis

Based on petrographic observation, pyrite-bearing rocks were sliced and later polished by the polishing papers to get smooth surfaces for in situ sulfur isotope analysis. Sulfur isotope ratios of the pyrite were measured using a Thermo Fisher Scientific Neptune Plus MC-ICP-MS connected to an Electro Scientific Industries NWR193 193 nm ArF excimer laser-ablation system at State Key Laboratory for Mineral Deposit Research, Nanjing University. During the measurement, the pyrite was ablated by the NWR193 excimer laser in the single spot ablation mode with the spot size of 25 μm, the repetition rate of 8 Hz and the energy fluence of 7 J/cm². The ablated particles were then transported to MC-ICP-MS for isotope analysis with He as the carrier gas. The MC-ICP-MS was running with medium mass resolution setting to resolve polyatomic interferences of $^{16}O^{16}O^+$ and $^{16}O^{18}O^+$ on $^{32}S^+$ and $^{34}S^+$, respectively. The standard-sample-standard bracketing method was used to correct for the instrumental mass bias and the standard used was pyrite WS-1 whose $\delta^{34}S_{V-CDT}$ value is 0.3±0.1‰ (Zhu *et al.*, 2017). Each sulfur isotope ratio measurement took about 70s (140 integrations with an integration time of 0.524s), comprising a 20s measurement of baseline (which would be removed by on-peak subtraction), 30s analysis of the standard or samples, and the last 20s for aerosol washout. The typical internal precision (2SE) was better than 0.20‰ for $^{34}S/^{32}S$. Sulfur isotope compositions are reported as $\delta^{34}S$ values relative to Vienna - Cañon Diablo Troilite (V-CDT). The accuracy of the method was assessed by analyses of well-characterized sulfide standards (Balmat sphalerite, $\delta^{34}S$=15.42±0.14‰, 2SD, Kozdon *et al.*, 2010; AgS standard, $\delta^{34}S$=0.07±0.26‰, 2SD, Ding *et al.*, 2001). Despite the difference in matrix, the measured $\delta^{34}S$ values are consistent with the certified values of the respective samples within ±0.5‰ (i.e., Balmat sphalerite, $\delta^{34}S$=15.77±0.36‰, 2SD, n=6, this study; AgS standard, $\delta^{34}S$=-0.51±0.46‰, 2SD, n=5, this study). 0.5‰ is also the 2SD error in $\delta^{34}S$ for repeated analysis on the same sulfide. Therefore, the external analytical uncertainty of our method for $\delta^{34}S$ is estimated to be better than ±0.5‰, such uncertainty is sufficiently small to resolve the >40‰ variability in the Xinyu samples.

Table S-1 Comparison of Fe isotope compositions for USGS rock standards measured in this study with literature values.

Sample	$\delta^{56}Fe$	2SD	$\delta^{57}Fe$	2SD	N
Fe isotope compositions of USGS rock standards measured in this study					
DTS-2b	0.06	0.08	0.08	0.14	3
BHVO-2	0.13	0.05	0.21	0.13	9
BCR-2	0.11	0.08	0.18	0.12	9
Fe isotope compositions of USGS rock standards in literature					
DTS-2b (Craddock and Dauphas, 2011)	0.028	0.042	0.045	0.047	6
BHVO-2 (Craddock and Dauphas, 2011)	0.114	0.035	0.174	0.046	12
BHVO-2 (He *et al.*, 2015)	0.112	0.021	0.163	0.040	27
BHVO-2 (Liu *et al.*, 2014)	0.121	0.049	0.175	0.064	12
BCR-2 (Craddock and Dauphas, 2011)	0.091	0.032	0.126	0.066	8
BCR-2 (He *et al.*, 2015)	0.080	0.024	0.123	0.036	10
BCR-2 (Liu *et al.*, 2014)	0.107	0.025	0.170	0.013	3

Table S-2 Composition of the selected interstitial carbonates in Xinyu IF samples as measured by electron microprobe.

Analysis No.	MnO (wt.%)	MgO (wt.%)	ZnO (wt.%)	SrO (wt.%)	CaO (wt.%)	FeO (wt.%)	Total (wt.%)
1	0.54	10.10	0.05	0.25	29.55	15.42	55.91
2	1.56	12.83	-	0.11	29.55	10.50	54.55
3	1.56	12.71	0.02	0.13	28.97	10.89	54.27
4	0.54	9.99	0.10	0.28	31.59	13.65	56.14
5	1.64	12.88	-	0.12	29.48	11.52	55.64
6	1.39	12.77	-	0.05	29.27	11.26	54.75
7	1.42	12.79	0.01	0.20	28.87	11.19	54.47
8	1.56	13.25	-	0.08	29.67	10.55	55.12
9	1.46	13.37	-	0.09	28.81	11.20	54.92
10	1.44	13.05	0.10	0.17	28.83	11.91	55.49
11	1.31	12.31	-	0.24	28.80	12.00	54.65
12	1.32	13.02	0.05	0.11	28.87	11.32	54.69
13	2.22	1.52	0.03	0.29	52.51	1.63	58.19

14	3.05	0.15	0.06	0.09	55.82	0.37	59.54
15	2.97	8.81	0.11	0.19	27.64	15.69	55.40
16	3.95	8.16	0.03	0.30	28.30	15.13	55.86
17	1.28	7.38	0.02	0.12	30.62	18.94	58.36
18	3.10	8.01	0.14	0.19	27.09	17.98	56.50
19	3.33	8.01	0.03	0.18	27.49	16.86	55.90
20	3.54	7.52	-	0.18	27.20	17.54	55.98
21	3.10	7.68	0.04	0.18	26.75	17.80	55.54
22	1.47	6.95	-	0.23	28.40	19.08	56.13
23	3.81	7.57	0.06	0.09	27.09	17.30	55.92
24	2.75	8.76	0.03	0.22	27.76	15.65	55.17
25	17.05	9.52	0.01	0.09	26.49	7.68	60.81
26	16.39	8.59	0.05	0.12	26.52	8.98	60.63
27	15.25	8.98	-	0.11	24.19	6.59	55.12
28	15.79	8.26	-	0.07	26.05	8.14	58.30
29	15.94	9.07	0.01	0.16	24.98	7.09	57.24
30	17.82	9.03	-	0.19	26.65	8.26	61.94
31	17.05	9.75	0.06	0.08	27.53	8.12	62.58
32	16.82	8.91	0.02	0.13	24.25	6.89	57.00

Table S-3 Iron, sulfur and carbon isotope composition for Iron formations of the Xinyu IF.

Samples	Depth (m)	$\delta^{56}Fe$ (‰)	2SD	$\delta^{57}Fe$ (‰)	2SD	N	$\delta^{13}C$ (‰, PDB)	2SD	N	$\delta^{34}S$ (‰, CDT)	2SE
Chlorite muscovite schist of the upper Shangshi formation											
ZK11605-02	59.6	0.12	0.03	0.2	0.05	1					
ZK11605-03	94.0	0.09	0.02	0.17	0.04	1					
Carbonaceous pseudo-conglomerate-contained chlorite sericite phyllite of Gujia Formation											
ZK11605-04	114.6	0.11	0.02	0.28	0.05	1	-6.54	0.03	3		
ZK11605-05	114.7	0.15	0.02	0.24	0.04	1	-6.48	0.13	1		
ZK11605-06	114.8						-6.81	0.07	1		
ZK11605-07	117.0	0.19	0.02	0.25	0.04	1					
Magnetite-bearing chlorite sericite phyllite of the fist member of Xiafang Formation											
ZK11605-08	120.7	0.06	0.02	0.13	0.04	1	-7.17	0.05	2		
ZK11605-09	125.6	0.22	0.02	0.39	0.04	1	-8.00	0.11	3		
ZK11605-10	136.9	0.39	0.02	0.69	0.05	1	-6.96	0.10	1		
ZK11605-11	160.4	0.14	0.02	0.19	0.04	1	-8.26	0.07	2		
ZK11605-12	166.0	-0.09	0.02	-0.14	0.05	1	-8.00	0.02	2		
ZK11605-13	174.8	-0.04	0.02	-0.08	0.05	1	-7.90	0.09	1		
ZK11605-14	177.5	-0.06	0.02	-0.06	0.04	1	-7.85	0.09	2		
ZK11605-15	184.5	0.21	0.03	0.40	0.05	1	-8.24	0.11	2		
ZK11605-16	184.8	0.27	0.03	0.40	0.05	1					
ZK11605-17	189.0	0.41	0.14	0.59	0.12	2	-8.41	0.06	1		
ZK11605-18	190.0	-0.02	0.01	-0.04	0.06	2	-8.69	0.12	1		
ZK11605-19	192.2						-6.71	0.03	1		
ZK11605-20	194.2	0.52	0.07	0.8	0.01	2	-8.29	0.05	1		
ZK11605-21	196.4	0.39	0.01	0.62	0.01	2					
ZK11605-22	197.0	0.95	0.02	1.41	0.02	2	-8.47	0.01	3		
Iron formation of the second member of Xiafang Formation											
ZK11605-23	197.9	0.08	0.04	0.10	0.00	2					
ZK11605-24	199.1	0.14	0.00	0.27	0.03	2					
ZK11605-25	201.1	0.35	0.02	0.49	0.14	2					

ZK11605-26	202.1	0.63	0.01	0.95	0.13	2					
ZK11605-27	202.9	0.16	0.05	0.26	0.22	2	-9.46	0.07	1		
ZK11605-28	204.4	0.78	0.01	1.16	0.07	2	-9.36	0.11	3		
ZK11605-29	205.5	1.53	0.04	2.26	0.07	2	-9.73	0.06	2		
ZK11605-30	206.5	1.67	0.01	2.49	0.02	2	-9.62	0.03	3		
ZK11605-32	208.7	1.61	0.06	2.4	0.03	2	-9.46	0.1	1		
ZK11605-33	209.7	1.55	0.00	2.35	0.03	2	-10.48	0.03	1		
ZK11605-34	210.7	2.10	0.20	3.17	0.02	2	-11.68	0.23	1		
ZK11605-36	214.7	1.01	0.02	1.41	0.02	2					

Pyrite-bearing sericite phyllite of the third and fourth members of Xiafang Formation

ZK11605-37	218.0	0.29	0.06	0.46	0.19	2	-7.07	0.02	2	-41.81	0.14
ZK11605-38	220.0	0.84	0.03	1.27	0.05	2	-7.19	0.08	2	-29.1	0.10
										-29.8	0.11
										-29.57	0.13
										-29.47	0.10
ZK11605-39	222.0	0.73	0.07	1.12	0.27	2	-9.09	0.08	2	-25.32	0.13
										-25.96	0.16
ZK11605-40	225.0	0.59	0.01	0.93	0.03	2	-8.08	0.09	1	-17.14	0.13
										-16.58	0.09
										-15.26	0.11
										-17.2	0.11
ZK11605-41	227.0	0.46	0.03	0.68	0.07	2	-7.42	0.18	1	-16.28	0.13
										-15.71	0.10
										-16.18	0.10
										-16.35	0.12
ZK11605-42	230.0	0.23	0.00	0.36	0.03	2	-7.60	0.02	3	-15.49	0.11
										-15.46	0.12
										-12.55	0.13
ZK11605-43	232.0	0.38	0.06	0.64	0.01	2	-7.64	0.07	1		
ZK11605-44	236.5	0.50	0.03	0.78	0.12	2	-7.40	0.01	2	-10.37	0.15
										-9.85	0.13
ZK11605-45	239.0									-4.33	0.23

ZK11605-46	240.0	0.37	0.00	0.50	0.22	2	-7.71	0.07	1	-4.24	0.16
										-3.92	0.13
ZK11605-47	243.0	0.24	0.00	0.41	0.1	2	-7.89	0.06	2	-14.98	0.13
										-14.83	0.19
ZK11605-48	245.5	0.29	0.03	0.45	0.05	2	-7.91	0.05	3	-10.38	0.12
										-12.01	0.15
ZK11605-49	246.0									-8.28	0.12
										-10.66	0.12
										-9.90	0.13
										-10.64	0.13
ZK11605-50	249.0	0.07	0.01	0.09	0.15	2	-6.42	0.07	1	-1.89	0.11
										-5.33	0.10
										-5.39	0.10
										-2.27	0.10
ZK11605-51	252.0	0.30	0.03	0.46	0.07	2	-8.03	0.05	1	1.17	0.13
										1.26	0.13
										0.81	0.13
										1.44	0.13
ZK11605-52	254.0	0.80	0.08	1.25	0	2	-7.9	0.08	1	3.21	0.14
										3.83	0.13
										3.47	0.14
										3.16	0.12
ZK11605-53	257.0									3.01	0.15
										2.16	0.12
										2.42	0.10
										2.88	0.10
ZK11605-54	260.0									3.10	0.12
										2.86	0.12
										2.94	0.12
										2.88	0.13
ZK11605-55	263.0									4.19	0.10
										4.48	0.11

									4.72	0.11
									4.34	0.19
ZK11605-56	266.5								5.07	0.12
									5.16	0.11
									3.91	0.11
									4.35	0.13
ZK11605-57	268.0								1.76	0.12
									1.92	0.13
									1.76	0.12
									1.59	0.13
ZK11605-58	270.0	0.42	0.02	0.61	0.11	2	-7.85	0.1	1	0.97	0.13
									0.97	0.18
									0.76	0.13
									1.07	0.15
ZK11605-59	272.0	0.34	0.07	0.57	0.11	2	-7.99	0.07	2	-0.68	0.12
									-0.89	0.13
									-0.94	0.13
									-1.00	0.11

Supplementary Information References

Bao, X., Zhang, S., Jiang, G., Wu, H., Li, H., Wang, X., An, Z. Yang, T. (2018) Cyclostratigraphic constraints on the duration of the Datangpo Formation and the onset age of the Nantuo (Marinoan) glaciation in South China. *Earth and Planetary Science Letters* 483, 52–63.

Busigny, V., Planavsky, N.J., Goldbaum, E., Lechte, M.A., Feng, L., Lyons, T.W. (2018) Origin of the Neoproterozoic Fulu iron formation, South China: Insights from iron isotopes and rare earth element patterns. *Geochimica et Cosmochimica Acta* 242, 123–142.

Chen, D., Wang, J., Qing, H., Yan, D., Li, R. (2009) Hydrothermal venting activities in the Early Cambrian, South China: petrological, geochronological and stable isotopic constraints. *Chemical Geology* 258, 168–181.

Condon, D., Zhu, M., Bowring, S., Wang, W., Yang, A., Jin, Y. (2005) U-Pb ages from the neoproterozoic Doushantuo Formation, China. *Science* 308, 95–98.

Craddock P.R., Dauphas N. (2011) Iron isotopic compositions of geological reference materials and chondrites. *Geostandards And Geoanalytical Research* 35, 101–123.

Ding, T., Vaikiers, S., Wan, D., Bai, R., Zou, X., Li, Y., Zhang, Q., De Bievre, P. (2001) The 33S and 34S values and absolute 32S/33S and 32S/34S ratios of IAEA and Chinese sulfur isotope reference materials (in Chinese with English abstract). Bulletin of Mineralogy, *Petrology and Geochemistry* 20, 425–427.

Du, D.H., Wang, X.L., Yang, T., Chen, X., Li, J.Y., Li, W. (2017) Origin of heavy Fe isotope compositions in high-silica igneous rocks: A rhyolite perspective. *Geochimica et Cosmochimica Acta* 218, 58–72.

Eisbacher, G.H. (1985) Late Proterozoic rifting, glacial sedimentation, and sedimentary cycles in the light of Windermere deposition, western Canada. *Palaeogeography, Palaeoclimatology, Palaeoecology* 51, 231–254.

Gao, L.Z., Chen, J.S., Dai, C.G., Ding, X.Z., Wang, X.H., Liu, Y.X. (2014). SHRIMP zircon U-Pb dating of tuff in Fanjingshan Group and Xiajiang Group from Guizhou and Hunan Provinces and its stratigraphic implications. *Geological Bulletin of China*, 33(7), 949-959.

Gao, L.Z., Lu, J.P., Ding, X.Z., Wang, H.R., Liu, Y.X., Li, J. (2013) Zircon U–Pb dating of Neoproterozoic tuff in South Guangxi and its implications for stratigraphic correlation. *Geology in China* 40(5), 1443–1452.

Gao, W., Zhang, C.H. (2009) Zircon SHRIMP U-Pb ages of the Huangling granite and the tuff beds from Liantuo Formation in the Three Gorges area of Yangtze River, China and its geological significance. *Geological Bulletin of China* 28, 45–50.

Ge, W. C., Li, X.H., Li, Z.X., Zhou, H.W. (2001) Mafic intrusions in Longsheng area: age and its geological implications. *Chinese Journal of Geology* 36, 112–118 (in Chinese with English abstract).

Heimann, A., Johnson, C.M., Beard, B.L., Valley, J.W., Roden, E.E., Spicuzza, M.J., Beukes, N.J. (2010) Fe, C, and O isotope compositions of banded iron formation carbonates demonstrate a major role for dissimilatory iron reduction in ~ 2.5 Ga marine environments. *Earth and Planetary Science Letters* 294, 8–18.

Hoffman, P.F. Li, Z.X., (2009) A palaeogeographic context for Neoproterozoic glaciation. *Palaeogeography Palaeoclimatology Palaeoecology* 277, 158–172.

Hu, Z.Y., Hu, W.X., Wang, X.M., Lu, Y.Z., Wang, L.C., Liao, Z.W., Li, W.Q. (2017) Resetting of Mg isotopes between calcite and dolomite during burial metamorphism: Outlook of Mg isotopes as geothermometer and seawater proxy. *Geochimica et Cosmochimica Acta* 208, 24–40.

Huberty, J.M., Konishi, H., Heck, P.R., Fournelle, J.H., Valley, J.W., Xu, H. (2012) Silician magnetite from the Dales Gorge Member of the Brockman Iron Formation, Hamersley Group, Western Australia. *American Mineralogist* 97, 26–37.

Ilyin, A.V. (2009) Neoproterozoic banded iron formations. *Lithology and Mineral Resources* 44, 78–86.

Jiang, G., Kennedy, M.J., Christie-Blick, N., Wu, H., Zhang, S. (2006) Stratigraphy, sedimentary structures, and textures of the late Neoproterozoic Doushantuo cap carbonate in South China. *Journal of Sedimentary Research* 76, 978–995.

Jiang, G., Shi, X., Zhang, S., Wang, Y., Xiao, S. (2011) Stratigraphy and paleogeography of the Ediacaran Doushantuo Formation (ca. 635-551 Ma) in South China. *Gondwana Research* 19, 831–849.

Jiang, G.Q., Sohl, L.E., Christie-Blick, N. (2003) Neoproterozoic stratigraphic comparison of the Lesser Himalaya (India) and Yangtze block (south China): Paleogeographic implications. *Geology* 31, 917–920.

Kozdon, R., Kita, N.T., Huberty, J.M., Fournelle, J.H., Johnson, C.A., Valley, J.W. (2010) In situ sulfur isotope analysis of sulfide minerals by SIMS: Precision and accuracy, with application to thermometry of ∼3.5Ga Pilbara cherts. *Chemical Geology* 275, 243-253.

Lan, Z., Li, X.H., Zhang, Q., Li, Q.L. (2015a) Global synchronous initiation of the 2nd episode of Sturtian glaciation: SIMS zircon U–Pb and O isotope evidence from the Jiangkou Group, South China. *Precambrian Research* 267, 28–38.

Lan, Z., Li, X.H., Zhu, M., Zhang, Q., Li, Q.L. (2015b) Revisiting the Liantuo Formation in Yangtze Block, South China: SIMS U–Pb zircon age constraints and regional and global significance. *Precambrian Research* 263, 123–141.

Lan, Z., Li, X., Zhu, M., Chen, Z.Q., Zhang, Q., Li, Q., Lu, D., Liu, Y., Tang, G. (2014) A rapid and synchronous initiation of the wide spread Cryogenian glaciations. *Precambrian Research* 255, 401–411.

Li, W., Huberty, J.M., Beard, B.L., Kita, N.T., Valley, J.W., Johnson, C.M. (2013) Contrasting behavior of oxygen and iron isotopes in banded iron formations revealed by in situ isotopic analysis. *Earth and Planetary Science Letters* 384, 132–143.

Li, Z.X., Li, X.H., Kinny, P.D., Wang, J., Zhang, S., Zhou, H. (2003) Geochronology of Neoproterozoic syn-rift magmatism in the Yangtze Craton, South China and correlations with other continents: evidence for a mantle superplume that broke up Rodinia. *Precambrian Research* 122, 85–109

Liu S. A., Li D., Li S., Teng F. Z., Ke S., He Y., Lu, Y. (2014) High-precision copper and iron isotope analysis of igneous rock standards by MC-ICP-MS. *Journal of Analytical Atomic Spectrometry* 29, 122–133.

Ma, G., Li, H., Zhang, Z. (1984) An investigation of the age limits of the Sinian System in South China. *Bulletin of Yichang Institute of Geology and Mineral Resources* 8, 1–29.

Macdonald, F.A., Schmitz, M.D., Crowley, J.L., Roots, C.F., Jones, D.S., Maloof, A.C., Strauss, J.V., Cohen, P.A., Johnston, D.T., Schrag, D.P. (2010) Calibrating the cryogenian. *Science* 327(5970), 1241–1243.

Meng, C., Wu, C., Qin, H., Chi, Z., Yang, Z., Lei, R., Lou, F., Xie, G. (2017) In situ major and trace element geochemistry of magnetite: implication for ore formation processes and mechanism of the Liangshan iron deposit, Xinyu, China. *Geological Journal of China Universities* 23, 181–193.

Shu, L.S., Faure, M., Yu, J.H., Jahn, B.M. (2011) Geochronological and geochemical features of the Cathaysia block (South China): New evidence for the Neoproterozoic breakup of Rodinia. *Precambrian Research* 187, 263–276.

Song, G., Wang, X., Shi, X., Jiang, G. (2017) New U-Pb age constraints on the upper Banxi Group and synchrony of the Sturtian glaciation in South China. *Geoscience Frontiers* 8, 1161–1173.

Tang, J., Fu, H., Yu, Z. (1987) Stratigraphy, type and formation conditions of the Late Precambrian banded iron ores in South China. *Chinese Journal of Geochemistry* 6, 331–341.

Wang, J. Li, Z.X. (2003) History of Neoproterozoic rift basins in South China: implications for Rodinia break-up. *Precambrian Research* 122, 141–158.

Wang, W., Zhou, M.F., Yan, D.P., Li, J.W. (2012) Depositional age, provenance, and tectonic setting of the Neoproterozoic Sibao Group, southeastern Yangtze Block, South China. *Precambrian Research* 192-95, 107–124.

Wang, X.C., Li, X.H., Li, Z.X., Li, Q.L., Tang, G.Q., Gao, Y.Y., Zhang Q.R., Liu, Y. (2012) Episodic Precambrian crust growth: evidence from U–Pb ages and Hf–O isotopes of zircon in the Nanhua Basin, central South China. *Precambrian Research* 222, 386–403.

Wang, X.L., Zhou, J.C., Griffin, W.L., Zhao, G., Yu, J.H., Qiu, J.S., Zhang, Y.J. Xing, G.F. (2014) Geochemical zonation across a Neoproterozoic orogenic belt: Isotopic evidence from granitoids and metasedimentary rocks of the Jiangnan orogen, China. *Precambrian Research* 242, 154–171.

Yang, M.G., Liu, Y.G., Huang, Z.Z., Wu, F.J., Song, Z.R. (2012) Subdivision of Meso-Neoproterozoic strata in Jiangxi and a correlation with the neighboring areas. *Geology in China* 39, 43–53.

Yao, P., Wang, K.N., Du, C.L., Lin, Z.T., Song, X. (1993) Records of China's iron ore deposits. Beijing, *Metallurgical Industry Press* pp 660.

He Y., Ke S., Teng F. Z., Wang T., Wu H., Lu Y., Li S. (2015) High-precision iron isotope analysis of geological reference materials by high-resolution MC-ICP-MS. *Geostandards And Geoanalytical Research* 39, 341–356.

Yu, J.H., O'Reilly, S.Y., Wang, L., Griffin, W.L., Zhou, M.-F., Zhang, M., Shu, L. (2010) Components and episodic growth of Precambrian crust in the Cathaysia Block, South China: Evidence from U-Pb ages and Hf isotopes of zircons in Neoproterozoic sediments. *Precambrian Research* 181, 97–114.

Zhang, Q.R., Li, X.H., Feng, L.J., Huang, J., Song, B. (2008) A new age constraint on the onset of the Neoproterozoic glaciations in the Yangtze Platform, South China. *The Journal of Geology* 116, 423–429.

Zhang, S., Jiang, G., Han, Y. (2008) The age of the Nantuo Formation and Nantuo glaciation in South China. *Terra Nova* 20, 289–294.

Zhang, S., Jiang, G., Dong, J., Han, Y., Wu, H. (2008) New SHRIMP U-Pb age from the Wuqiangxi Formation of Banxi Group: Implications for rifting and stratigraphic erosion associated with the early Cryogenian (Sturtian) glaciation in South China. *Science in China Series D: Earth Sciences* 51, 1537–1544.

Zhao, G., Cawood, P.A. (2012) Precambrian geology of China. *Precambrian Research* 222, 13–54.

Zhao, G.C., Wilde, S.A., Cawood, P.A., Sun, M. (2001) Archean blocks and their boundaries in the North China Craton: lithological, geochemical, structural and P-T path constraints and tectonic evolution. *Precambrian Research* 107, 45–73.

Zheng, J.P., Griffin, W.L., O'Reilly, S.Y., Zhang, M., Pearson, N., Pan, Y.M. (2006) Widespread Archean basement beneath the Yangtze craton. *Geology* 34, 417–420.

Zhou, C., Huyskens, M.H., Lang, X., Xiao, S., Yin, Q.Z. (2019) Calibrating the terminations of Cryogenian global glaciations. *Geology* 47, 251–254.

Zhou, C.M., Tucker, R., Xiao, S.H., Peng, Z.X., Yuan, X.L., Chen, Z. (2004) New constraints on the ages of Neoproterozoic glaciations in south China. *Geology* 32, 437–440.

Zhou, J., Li, X. H., Ge, W., Li, Z.X. (2007) Age and origin of middle Neoproterozoic mafic magmatism in southern Yangtze Block and relevance to the break-up of Rodinia. *Gondwana Research* 12, 184–197.

Zhu, Z.-Y., Jiang, S.-., Ciobanu, C.L., Yang, T., Cook, N.J. (2017) Sulfur isotope fractionation in pyrite during laser ablation: Implications for laser ablation multiple collector inductively coupled plasma mass spectrometry mapping. *Chemical Geology* 450, 223-234.